Title	Achieving high specific charge capacitances in Fe3O4/reduced graphene oxide nanocomposites.
Author(s)	Shi, Wenhui.; Zhu, Jixin.; Sim, Dao Hao.; Tay, Yee Yan.; Lu, Ziyang.; Zhang, Xiaojun.; Sharma, Yogesh.; Srinivasan, Madhavi.; Zhang, Hua.; Hng, Huey Hoon.; Yan, Qingyu.
Citation	Shi, W., Zhu, J., Sim, D. H., Tay, Y. Y., Lu, Z., Zhang, X., et al. (2011). Achieving high specific charge capacitances in Fe3O4/reduced graphene oxide nanocomposites. Journal of Materials Chemistry, 21, 3422–3427.
Date	2011
URL	http://hdl.handle.net/10220/8360
Rights	© 2011 The Royal Society of Chemistry. This is the author created version of a work that has been peer reviewed and accepted for publication by Journal of Materials Chemistry, The Royal Society of Chemistry. It incorporates referee's comments but changes resulting from the publishing process, such as copyediting, structural formatting, may not be reflected in this document. The published version is available at: http://dx.doi.org/10.1039/c0jm03175e.

Achieving high specific charge capacitances in Fe_3O_4/reduced graphene oxide nanocomposites†

Wenhui Shi,[a] Jixin Zhu,[a] Dao Hao Sim,[a] Yee Yan Tay,[a] Ziyang Lu,[a] Xiaojun Zhang,[a] Yogesh Sharma,[b] Madhavi Srinivasan,[ab] Hua Zhang,[a] Huey Hoon Hng[a] and Qingyu Yan*[ab]

Received (in XXX, XXX) Xth XXXXXXXXX 20XX, Accepted Xth XXXXXXXXX 20XX
DOI: 10.1039/b000000x

We report a facile approach to synthesize nanocomposites with Fe_3O_4 nanopaticles (NPs) attached to reduced graphene oxide (rGO) sheets by a solvothermal process, which combines the growth of Fe_3O_4 NPs and the reduction of GOs in one single step. These Fe_3O_4/rGO nanocomposites were further used to fabricate thin film supercapacitor electrodes by using a spray deposition technique without the addition of insulating binders. It was found that the Fe_3O_4/rGO nanocomposites showed much higher specific capacitances than that of either pure rGO or pure Fe_3O_4 NPs. We further carried out electrochemical characterization of the Fe_3O_4/rGO nanocomposites with different Fe_3O_4 : rGO weight ratios (*e.g.* $I_{Fe_3O_4 : rGO}$) and showed that Fe_3O_4/rGO nanocomposites with $I_{Fe_3O_4 : rGO} = 2.8$ exhibited the highest specific capacitance of 480 F g^{-1} at a discharge current density of 5 A g^{-1} with the corresponding energy density of 67 W h kg^{-1} at a power density of 5506 W kg^{-1}. These Fe_3O_4/rGO nanocomposites also showed stable cycling performance without any decrease in the specific capacitance after 1000 charge/discharge cycles.

Introduction

Electrochemical capacitors (also known as supercapacitors or ultracapacitors) have drawn increasing attention for energy storage applications owing to their high power density, high rate capacity and long cycling life.[1–4] They have been proposed to play important roles in complementing or even replacing batteries in various applications ranging from portable electronics to hybrid electric vehicles.[5] Up till now, there are mainly three types of materials that may be used as supercapacitor electrode materials, *e.g.* carbonaceous materials,[6–11] transition metal oxides[12–21] and conductive polymers.[22–24] Carbonaceous materials are mainly used for electric double-layer capacitors, where the charge storage process is non-Faradic and the storage of energy is electrostatic. The keys to achieving high capacitance in electrical double layer capacitors are to increase the surface area and electrical conductivity. Recently, graphene has emerged as a promising material for electrochemical energy storage applications due to its chemical stability, unique mechanical strength, high electrical conductivity and high surface area.[25–29] The bulky paper made from graphene sheets also allows fabrication of a binder free flexible electrode without extra current collectors that may eliminate the contact resistance between the electrodes and current collectors.[26,27,30,31]

The energy storage mechanism for transition metal oxides, *e.g.* MnO_2,[14–16] RuO_2,[17,20] NiO[19] or SnO_2,[21] is mainly Faradic, which can realize large pseudocapacitance. However, the relatively low conductivity and poor stability of such materials usually requires the addition of conductive phases, *e.g.* carbon black or acetylene black, to enhance the charge transfer. Among the transition metal oxides, Fe_3O_4 is one of the more promising electrode materials due to its low cost and low environment impact. It also has a relatively high theoretical Li storage capacity,[32] which suggests that Fe_3O_4 may offer high pseudo charge capacitance through redox reaction. Previous studies on Fe_3O_4 as supercapacitor electrodes have shown low capacitances of 60–80 F g^{-1},[13,33] which is mainly due to its low electrical conductivity to enable effective ion diffusion. Blending Fe_3O_4 with conductive phases, *e.g.* carbon nanotubes, to form composites can effectively increase the total capacitance, to as high as 165 F g^{-1} at a current density of 0.2 A g^{-1}.[34]

Nanocomposites of graphene and metal oxide[28,35–38] for supercapacitor applications have attracted wide attention recently due to their synergistic effects by combining the redox reaction of metal oxide and high surface area/conductivity of graphene to improve the electrochemical performance.[39] Although high specific capacitances have been demonstrated in several composites, *e.g.* graphene–MnO_2 composites as supercapacitor electrodes,[31,40] it is worthwhile pointing out that the weight ratio between the graphene and the metal oxide should be tuned to optimize the electrochemical performance of the composite, which has not been well studied.

Herein, we report a facile approach to synthesize nanocomposite with Fe_3O_4 nanopaticles (NPs) attached to reduced graphene oxide (rGO) sheets, which combines the growth of Fe_3O_4 NPs and the reduction of graphene oxides (GOs) in one single step. These Fe_3O_4/rGO nanocomposites were further used to fabricate thin film supercapacitor electrodes by using a spray

[a]*School of Materials Science and Engineering, Nanyang Technological University, Singapore, 639798. E-mail: alexyan@ntu.edu.sg; Fax: + 65 6790 9081; Tel: + 65 6790 4583*
[b]*Energy research Institute @ NTU, Nanyang Technological University, Singapore, 639798*

† Electronic supplementary information (ESI) available: Raman spectra of GO and rGO, TGA datas, XRD pattern of GO and rGO, BET, galvanostatic charge/discharge curves and EIS spectra of Fe_3O_4/rGO nanocomposite. See DOI: 10.1039/c0jm03175e/

deposition technique without the addition of insulating binders. It was found that the Fe_3O_4/rGO nanocomposites showed much higher specific capacitances than that of either pure rGO or pure Fe_3O_4 NPs. We further investigated the Fe_3O_4/rGO nanocomposites with different Fe_3O_4 : rGO ratios. It was shown that Fe_3O_4/rGO nanocomposites with 73.5% Fe_3O_4 NPs showed the highest specific capacitance of 480 F g^{-1} at a discharge current density of 5 A g^{-1} with the corresponding energy density of 67 W h kg^{-1} at a power density of 5506 W kg^{-1}. These Fe_3O_4/rGO nanocomposites also showed stable cycling performance without any decrease in the specific capacitance after 1000 charge/discharge cycles.

Experimental

Materials

Natural graphite was purchased from Bay Carbon (Bay City, Michigan) and used for synthesizing graphene oxide(GO). H_2O_2 (30%), H_2SO_4 (98%), ferric chloride hexahydrate ($FeCl_3 \cdot 6H_2O$), phosphorpentoxid (97%), potassium persulfate ($K_2S_2O_8$), HCl (37%), potassium permanganate ($KMnO_4$), ferric chloride hexahydrate ($FeCl_3 \cdot 6H_2O$), ferrous chloride tetrahydrate ($FeCl_2 \cdot 4H_2O$), ethanol, ammonia solution ($NH_3 \cdot H_2O$) 25% were purchased from Sigma-Aldrich. All chemicals were used as received without any further purification. Millipore water was used in all experiments.

Synthesis of graphene oxides (GOs)

Graphene oxide was synthesized from natural graphite by a modified Hummers method, as described elsewhere.[41–43] In brief, 0.3 g of graphite was added into a mixture of 2.4 mL of 98% H_2SO_4, 0.5 g of $K_2S_2O_8$, and 0.5 g of P_2O_5, and the solution was kept at 80 °C for 4.5 h. The resulting preoxidized product was cleaned by water and dried. After the preoxidized product was added into 12 mL of 98% H_2SO_4, followed by slow addition of 1.5 g of $KMnO_4$ with the temperature kept at <20 °C in order to avoid overheating and explosion, the solution temperature was increased to 35 °C and maintained for 2 h. Then, 25 mL of H_2O was added. After 2 h, an additional 70 mL of H_2O was added to dilute the solution, and 2 mL of 30% H_2O_2 was injected into the solution to completely react with the excess $KMnO_4$. A bright yellow solution was obtained. Then, the resulting mixture was washed by HCl and H_2O, and the graphite oxide was obtained. The obtained graphite oxide was dispersed in water with a certain concentration and subsequently sonicated to obtain GOs.

Synthesis of Fe_3O_4/reduced graphene oxide (rGO)

20 mL GOs in water suspension (a concentration of ~0.25 mg mL^{-1}) were heated to 70 °C with magnetic stirring. An aqueous solution of $FeCl_3 \cdot 6H_2O$ and $FeCl_2 \cdot 4H_2O$ was injected in. The mixture was kept at 70 °C and stirred overnight under N_2 atmosphere. Then, 3 mL $NH_3 \cdot H_2O$ was added dropwisely into the solution. The mixture was loaded into a 50 ml Teflon lined stainless steel autoclave for hydrothermal reaction at 150 °C for 2 h. The final product was washed with ethanol and water, and dried in oven at 60 °C for 12 h. Different weight ratios of Fe_3O_4 to rGO were prepared by varying the amount of $FeCl_3 \cdot 6H_2O$ and $FeCl_2 \cdot 4H_2O$ added during the synthesis process. For comparison, samples of pure Fe_3O_4 and pure rGO were also prepared using a similar method.

Characterization

The morphology of the samples was investigated using a field emission scanning electron microscope (JEOL, Model JSM-7600F). Transmission electron microscopy (TEM) images were taken by using a JEOL 2010F operated at 200 kV. The crystal structural characterization of the samples was carried out using a Scintag PAD-V X-ray diffractometer at a scan rate of 1°/s with a 2θ range of 10–80° with Cu $K_{\alpha 1}$ radiation ($\lambda = 0.15406$ nm). The Raman spectra were obtained by using a WITec CRM200 confocal Raman microscopy system with a laser wavelength of 488 nm and spot size of 0.5 nm. To calibrate the wavenumber, the Si peak at 520 cm^{-1} was used as a reference. The electrical conductivity of these materials was measured by a four-point probe method. The composition of Fe_3O_4/rGO nanocomposites were determined by the thermal gravimetric analysis using a TA Instruments Q500 Thermogravimetric Analyzer (TGA) with a heating rate of 5 °C min^{-1} under dry air. The specific surface areas were investigated by using the Brunauer–Emmet–Teller (BET) methods.

Electrochemical testing

To fabricate film electrodes, the Fe_3O_4 NPs, rGO and Fe_3O_4/rGO nanocomposites were dispersed in ethanol. The suspensions were then spray deposited onto 2 × 1 cm carbon papers. The electrodes were dried under vacuum at room temperature for 6 h. The electrochemical properties and capacitance measurements of the supercapacitor electrodes were studied in a three-electrode half-cell system in 1 M KOH electrolyte with Solartron analytical equipment (Model 1470*E*). Platinum wire was used as a counter electrode and Ag/AgCl as the reference electrode. Electrochemical impedance spectroscopy (EIS) measurements were carried out in the frequency range from 10 kHz to 0.1 Hz at open circuit potential with an ac perturbation of 10 mV with the help of an impedance spectrum analyzer (Solatron, SI 1255B Impedance/gain-phase analyzer; computer software ZView).

Results and discussion

Scanning electron microscopy (SEM) and transmission electron microscopy (TEM) images (see Fig. 1a and b) show the representative morphology of the nanocomposite sample prepared with a precursor mass ratio of $FeCl_3 \cdot 6H_2O$: $FeCl_2 \cdot 4H_2O$: graphene oxides (GOs) = 10 : 4 : 5, which reveal that there are nanoparticles (NPs) of 4–8 nm uniformly decorated onto the thin sheets. The selected area electron diffraction (SAED) pattern (see inset in Fig. 1b) and high resolution TEM image (see Fig. 1c) of these NPs reveal that these particles are magnetite Fe_3O_4 with a face-centered cubic crystal structure (JCPDS 89-4319). The reduction of graphene oxides (GOs) was examined by Raman spectroscopy (see ESI Fig. S1†) and electrical conductivity measurements. Fig. S1† shows the increase in the intensity ratio of D band (located at 1350 cm^{-1}) and G band (located at 1580 cm^{-1}), *e.g.* I_D/I_G, from

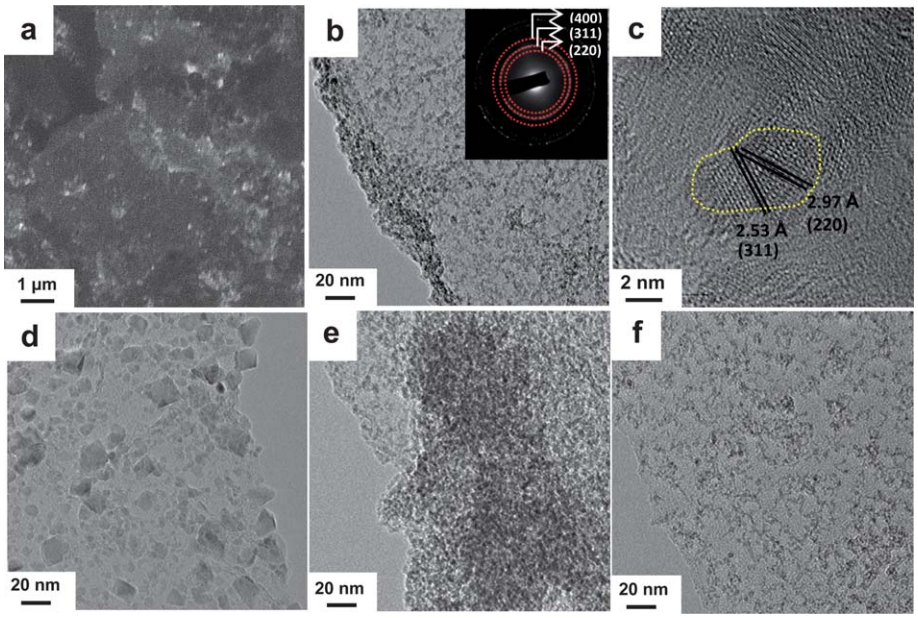

Fig. 1 (a) SEM (b) TEM and (c) HRTEM images of as-prepared Fe_3O_4/rGO nanocomposites prepared with a precursor weight ratio of $FeCl_3 \cdot 6H_2O$: $FeCl_2 \cdot 4H_2O$: GOs = 10 : 4 : 5 (the inset in b is the SAED pattern of Fe_3O_4 nanoparticles) (d–f) TEM images of Fe_3O_4/rGO nanocomposites prepared with precursor ratios of $FeCl_3 \cdot 6H_2O$: $FeCl_2 \cdot 4H_2O$: GOs = (d) 20 : 9 : 1, (e) 6 : 3 : 5, and (f) 5 : 2 : 10, respectively.

0.91 to 1.36 upon the reduction of GOs through the solvothermal process, which is consistent with previous reports.[44] Meanwhile, the four-point-probe measurements show that the GO films on glass is insulating and the as-prepared nanocomposites depict a high electrical conductivity of 800 S m^{-1}. The TEM images of samples prepared with various precursor ratios are shown in Fig. 1d–f. Large NPs of 10–20 nm are observed in the sample prepared with a precursor ratio of $FeCl_3 \cdot 6H_2O$: $FeCl_2 \cdot 4H_2O$: GOs = 20 : 9 : 1 while only smaller particles of 4–8 nm are detected in the other samples. The large Fe_3O_4 NPs observed in samples prepared with higher Fe precursors are possibly formed through the coarsening of the smaller NPs.

Here, for samples prepared with different precursor ratios, we have estimated the weight ratio of Fe_3O_4 : rGO in the nanocomposites, $I_{Fe_3O_4 : rGO}$, by thermal gravimetric analysis (TGA) in air (see ESI Fig. S2†). The XRD measurements indicate that the final residue is only Fe_2O_3 (Fe_3O_4 oxidized to Fe_2O_3) after heating the samples to above 500 °C in air, based on which we calculated the weight ratio to be $I_{Fe_3O_4 : rGO}$ = 19.8, 5, 2.8 and 0.8 for samples prepared with precursor ratios of $FeCl_3 \cdot 6H_2O$: $FeCl_2 \cdot 4H_2O$: GOs = 20 : 9 : 1, 6 : 3 : 5, 10 : 4 : 5 and 5 : 2 : 10, respectively. Here, in the TGA curves, the first 5% weight loss at the temperature below 100 °C is attributed to the evaporation of moisture.

Fig. 2 shows the representative X-ray diffraction patterns of nanocomposites with different $I_{Fe_3O_4 : rGO}$ values, which confirms the formation of magnetite Fe_3O_4 (JCPDS 89-4319) and is consistent with the SAED and HRTEM observations. For GOs, a sharp peak at the $2\theta \sim 10.8°$ is observed (see ESI Fig. S3†) in the XRD pattern, which corresponds to the (001) reflection. The estimated interlayer spacing of GO using the Scherrer equation[45] is around 0.82 nm. The sharp peak disappears upon reducing the GOs to rGO and only a broad hump at 2θ between 20° and 30° remains due to a relatively short domain order or turbostratic arrangement of the rGO stacked sheets.[46,47]

The specific surface area of the Fe_3O_4/rGO nanocomposites was investigated by BET techniques. Based on the hysteresis loop obtained in the N_2 gas adsorption-desorption isotherm (see ESI Fig. S4†), the surface area calculated for Fe_3O_4/rGO nanocomposites with $I_{Fe_3O_4 : rGO}$ = 2.8 is around 192 m^2 g^{-1} as compared to 42 m^2 g^{-1} for pure Fe_3O_4 NPs, which is mainly due to the large surface area of the rGO sheets.

The electrochemical performance of the electrodes made from Fe_3O_4/RGO nanocomposites was investigated by cyclic voltammogram (CV) and galvanostatic charge/discharge measurements within the potential range of −0.8–0.2 V in 1 M KOH aqueous solution. The CV curve (see Fig. 3a) of Fe_3O_4/rGO nanocomposites with $I_{Fe_3O_4 : rGO}$ = 2.8, clearly shows the pair of cathodic and anodic peaks, which correspond to the reversible

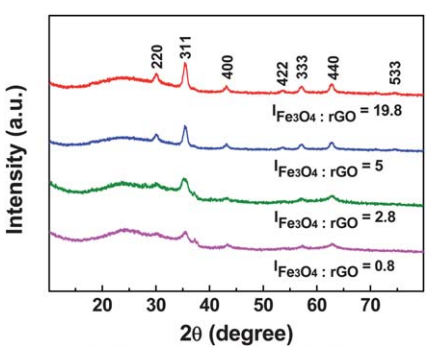

Fig. 2 X-ray diffraction patterns of Fe_3O_4/rGO nanocomposites with different $I_{Fe_3O_4 : rGO}$ values.

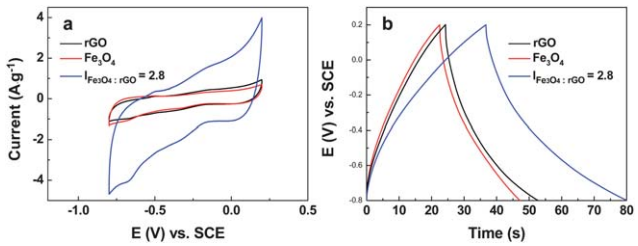

Fig. 3 (a) Cyclic voltammogram curves of Fe_3O_4 NPs, rGO and nanocomposites with $I_{Fe_3O_4 : rGO} = 2.8$ at a scan rate of 5 mV s^{-1} in 1 M KOH (b) Galvanostatic charge/discharge curves of rGO, Fe_3O_4 and nanocomposite with $I_{Fe_3O_4 : rGO} = 2.8$ in 1 M KOH solution at 5 A g^{-1}.

reactions of Fe(II) ↔ Fe(III).[33,48] The CV curves of pure Fe_3O_4 NPs and pure rGO at the same scan rate are also plotted in Fig. 3a, which are much narrower than that of the Fe_3O_4/rGO nanocomposites and indicate smaller specific capacitances.

The specific capacitances C_s were calculated from the corresponding galvanostatic discharge curves (see Fig. 3b) using the equation as follows:

$$C_s = \frac{I}{-\left(\frac{\Delta E}{\Delta t}\right)m}$$

where $(\Delta E/\Delta t)$ is the average slope of the discharge curve after the IR drop, Δt is the discharge time, m is the active mass and I is the discharge current. The calculated specific capacitances are 480 F g^{-1} for nanocomposites with $I_{Fe_3O_4 : rGO} = 2.8$ at a discharge current density of 5 A g^{-1}, which is much higher than that of pure Fe_3O_4 (*i.e.* 104 F g^{-1}) and rGO (*i.e.* 139 F g^{-1}) electrodes. The galvanostatic charge/discharge measurements at different current densities are also carried out for samples with different $I_{Fe_3O_4 : rGO}$ (see ESI Fig. S5†). For the same sample, decreasing the discharge current density results in higher specific capacitances, *e.g.* the value of Cs for nanocomposites with $I_{Fe_3O_4 : rGO} = 2.8$ increases from 480 F g^{-1} to 890 F g^{-1} upon decreasing the current density from 5 A g^{-1} to 1 A g^{-1}. Varying the $I_{Fe_3O_4 : rGO}$ values also leads to varied specific capacitances at different current densities, which is summarized in Fig. 4a. It clearly shows that Fe_3O_4/rGO nanocomposite with $I_{Fe_3O_4 : rGO} = 2.8$ depicts the highest specific capacitances among all the prepared samples at all tested current densities. For example, at a current density of 1 A g^{-1}, nanocomposite with $I_{Fe_3O_4 : rGO} = 2.8$ show the highest Cs value of 890 F g^{-1} while the values of C_s decreased to 582, 654, and 705 F g^{-1} for nanocomposites with $I_{Fe_3O_4 : rGO} = 19.8$, 5, and 0.8, respectively. The energy densities and power densities can be further calculated from these results (see Fig. 4b) using the following equations:

$$E = \frac{1}{2}C_s(\Delta V)^2$$

$$P = \frac{E}{t}$$

where E is the energy density, C_s is the specific capacitance, ΔV is the potential range, P is power density and t is the time to discharge. For nanocomposites with $I_{Fe_3O_4 : rGO} = 2.8$, the energy densities are 124, 93, 80 and 67 W h kg^{-1} at power densities of 1, 2, 3 and 5 A g^{-1}, respectively, which are higher than samples with other $I_{Fe_3O_4 : rGO}$ values. The cyclability of Fe_3O_4/rGO nanocomposite electrodes were also tested by continuous charge–discharge measurements at different current densities for different cycle numbers within a voltage range of −0.8–0.2 V. At a current density of 5 A g^{-1}, the specific capacitance of nanocomposites with $I_{Fe_3O_4 : rGO} = 2.8$ increases about 15% during the first 200 cycles and remains stable as the charge/discharge cycles increase to 1000 (see Fig. 5). At a current density of 10 A g^{-1}, the specific capacitance of the same composite show a similar trend, which increases about 12% for the first 2000 cycles and then remains stable till 10 000th cycles (see ESI Fig. S7†). Both results indicate the excellent cyclability of such a Fe_3O_4/rGO nanocomposite. The increase of C_s during the charge/discharge cycles is attributed to the activation process to allow the trapped cations to gradually diffuse out.[49]

The electrochemical impedance spectroscopy (EIS) is a non-destructive and useful technique for evaluation of the kinetic and mechanistic information of electrode materials. The data, in the form of Nyquist plots[50] (Z' *vs.* $-Z''$), (see Fig. 6a and ESI Fig. S7†), were collected in the frequency range of 10 kHz to 0.1 Hz using an ac bias of 10 mV. Z' and Z'' refer to the real and imaginary parts of complex impedance. Qualitatively, all spectra are similar in shape, where an arc in the high frequency region and inclined line in the low frequency region are seen. The arc usually attributes to the inter-particle resistance and charge transfer impedance.[26,36,51,52] The inclined portion of the curve (about 45°) in the middle frequency is ascribed to the Warburg

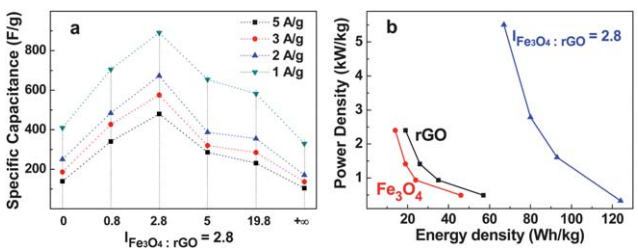

Fig. 4 (a) Specific capacitances of Fe_3O_4 NPs, rGO and nanocomposites with different $I_{Fe_3O_4 : rGO}$ values. (the x axis is the weight ratio of Fe_3O_4 to rGO, 0 represents pure rGO and $+\infty$ represents pure Fe_3O_4) (b) The energy densities and corresponding power densities of rGO, Fe_3O_4 NPs and Fe_3O_4/rGO nanocomposite with $I_{Fe_3O_4 : rGO} = 2.8$.

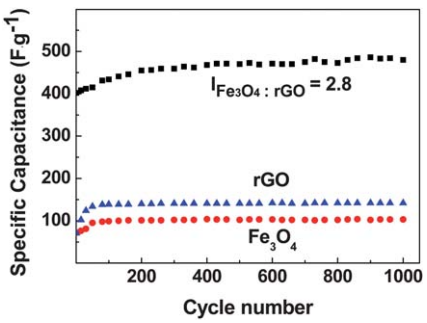

Fig. 5 The cycling performance of Fe_3O_4 NPs, rGO and the nanocomposite electrode with $I_{Fe_3O_4 : rGO} = 2.8$ at a current density of 5 A g^{-1} in 1 M KOH.

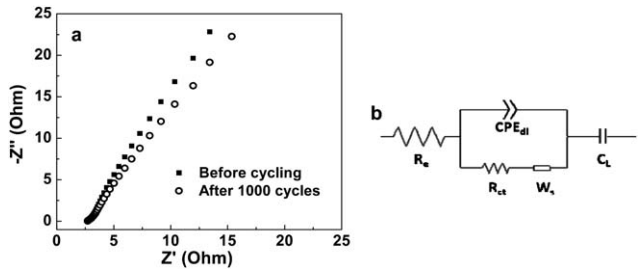

Fig. 6 (a) Nyquist plots of experimental impedance data for Fe_3O_4/rGO nanocomposite electrode with $I_{Fe_3O_4 : rGO} = 2.8$ in the frequency range of 10 kHz to 0.1 Hz. (b) The electrical equivalent circuit used for fitting of impedance spectra.

impedance, which is a consequence of the frequency dependence of ion diffusion/transport in the electrolyte to the electrode surface.[36,51] The experimental data are fitted with an equivalent circuit, shown in Fig. 6b, which consists of a series and parallel combination of resistances, R_e (contribution of ionic resistance of electrolyte, intrinsic resistance of substrate, and contact resistance between active material and current collector), R_{ct} (charge transfer resistance) constant phase element (CPE_{dl} : double layer capacitance), Warburg impedance, W_s and C_L (the limit capacitance). As can be seen in Fig. 6 and Table 1, the value of R_e remains almost constant 2.5 ($\pm$ 0.5) Ω for all the devices, which shows almost same behavior of the Fe_3O_4/rGO composite electrode. However, a significant variation in Warburg impedances is clearly observed. It is well-known that the proportion of the Warburg region in the Nyquist plot is the limiting factor for ion diffusion/transport from electrolyte to the electrode surface. The higher value of W_s reduces the access of electrolyte ions to the active electrode surface and indicates greater variation in ion diffusion path lengths and increased obstruction of ion movement.[51–53] This is therefore detrimental to good supercapacitor behavior. As is observed from Table 1, the value of W_s for the Fe_3O_4/rGO composite lies between the value of pure rGO and pure Fe_3O_4, therefore, the electrolyte access in Fe_3O_4/rGO composite may be relatively higher, which would facilitate the efficient access of electrolyte ions to the Fe_3O_4/rGO composite electrode and thus, will aid in delivering the high pseudocapacitance as compare to the pure Fe_3O_4. After 1000 cycles, an almost identical impedance curve is obtained, further demonstrating the long term electrochemical stability of the composite of rGO and Fe_3O_4.

Meanwhile, we examined the morphology of three types of electrodes (pure Fe_3O_4 electrode, pure rGO electrode and Fe_3O_4/rGO nanocomposite electrode with $I_{Fe_3O_4 : rGO} = 2.8$) before and after 1000 cycles by SEM (see ESI Fig. S8†). There is no obvious agglomeration of the nanostructures for all three types of electrodes after the cycling test, which is consistent with their stable cycling performance, as shown in Fig. 5. The crystal structures of the Fe_3O_4 NPs were investigated by TEM, HRTEM and SAED characterization (see ESI Fig. S9†). There is no clear coalescence of the NPs after 1000 charge/discharge cycles. The SAED pattern and HRTEM image reveal that these NPs are still magnetite Fe_3O_4 with face-centered cubic crystal structure (JCPDS 89-4319).

Table 1 The calculated values of R_e, R_{ct}, CPE_{dl}, W_s and C_L through fittings of the experimental impedance spectra based on the proposed equivalent circuit in Fig. 6b

		R_e (Ω)	R_{ct} (Ω)	CPE_{dl} (mF)	W_s	C_L (F)
Before Cycling	rGO	1.7	0.1	0.003	5.8	0.05
	Fe_3O_4	2	0.5	0.1	50	0.03
	Fe_3O_4/rGO	2.8	0.6	1.6	21.8	0.04
After 1000 Cycles	rGO	1.8	0.1	0.004	4.9	0.05
	Fe_3O_4	2.1	0.4	0.7	47	0.04
	Fe_3O_4/rGO	2.7	0.5	1.9	18.4	0.04

Conclusions

In summary, we have developed a simple solvothermal approach to synthesize Fe_3O_4/rGO nanocomposites, which combines the growth of Fe_3O_4 NPs and the reduction of GOs in one single step. When tested as supercapacitor electrodes, it was found that the Fe_3O_4/rGO nanocomposites showed much higher specific capacitances than that of either pure rGO or pure Fe_3O_4 NPs. Further investigating the Fe_3O_4/rGO nanocomposites with different Fe_3O_4 : rGO ratios, we found that the specific capacitance could be optimized by tuning the Fe_3O_4 : rGO ratios. It was shown that Fe_3O_4/rGO nanocomposites with 73.5% Fe_3O_4 NPs ($I_{Fe_3O_4 : rGO} = 2.8$) showed the highest specific capacitances at all tested current densities, *e.g.* 480 F g^{-1} at a discharge current density of 5 A g^{-1} with the corresponding energy density of 67 W h kg^{-1} at a power density of 5506 W kg^{-1}, and 843 F g^{-1} at a discharge current density of 1 A g^{-1} with the corresponding energy density of 124 W h kg^{-1} at a power density of 332 W kg^{-1}. These Fe_3O_4/rGO nanocomposites also showed stable cycling performance without any decrease in the specific capacitance after 10 000 charge/discharge cycles.

Acknowledgements

The authors gratefully acknowledge AcRF Tier 1 RG 31/08 of MOE (Singapore), NRF2009EWT-CERP001-026 (Singapore) and Singapore Ministry of Education (MOE2010-T2-1-017). H. Z. thanks the support of AcRF Tier 2 (ARC 10/10, No. MOE2010-T2-1-060) from MOE in Singapore. M.S. thanks the support of NRF-CRP4-2008-03 (Singapore).

Notes and references

1 Y. Zhang, H. Feng, X. B. Wu, L. Z. Wang, A. Q. Zhang, T. C. Xia, H. C. Dong, X. F. Li and L. S. Zhang, *Int. J. Hydrogen Energy*, 2009, **34**, 4889–4899.
2 L. P. Ma and Y. Yang, *Appl. Phys. Lett.*, 2005, **87**, 3.
3 M. Winter and R. J. Brodd, *Chem. Rev.*, 2004, **104**, 4245–4270.
4 X. J. Zhang, W. H. Shi, J. X. Zhu, W. Y. Zhao, J. Ma, S. Mhaisalkar, T. L. Maria, Y. H. Yang, H. Zhang, H. H. Hng and Q. Y. Yan, *Nano Research*, 3, pp. 643–652.
5 M. Kaempgen, C. K. Chan, J. Ma, Y. Cui and G. Gruner, *Nano Lett.*, 2009, **9**, 1872–1876.
6 K. S. Xia, Q. M. Gao, J. H. Jiang and J. Hu, *Carbon*, 2008, **46**, 1718–1726.
7 E. Frackowiak, *Phys. Chem. Chem. Phys.*, 2007, **9**, 1774–1785.
8 E. Frackowiak, K. Metenier, V. Bertagna and F. Beguin, *Appl. Phys. Lett.*, 2000, **77**, 2421–2423.
9 C. S. Du and N. Pan, *Nanotechnology*, 2006, **17**, 5314–5318.
10 L. L. Zhang and X. S. Zhao, *Chem. Soc. Rev.*, 2009, **38**, 2520–2531.

11 J. X. Zhu, T. Sun, H. H. Hng, J. Ma, F. Y. C. Boey, X. W. Lou, H. Zhang, C. Xue, H. Y. Chen and Q. Y. Yan, *Chem. Mater.*, 2009, **21**, 3848–3852.
12 N. L. Wu, *Mater. Chem. Phys.*, 2002, **75**, 6–11.
13 T. Cottineau, M. Toupin, T. Delahaye, T. Brousse and D. Belanger, *Appl. Phys. A: Mater. Sci. Process.*, 2006, **82**, 599–606.
14 J. H. Jiang and A. Kucernak, *Electrochim. Acta*, 2002, **47**, 2381–2386.
15 M. Toupin, T. Brousse and D. Belanger, *Chem. Mater.*, 2004, **16**, 3184–3190.
16 A. J. Roberts and R. C. T. Slade, *J. Mater. Chem.*, 2010, **20**, 3221–3226.
17 C.-C. Hu, K.-H. Chang, M.-C. Lin and Y.-T. Wu, *Nano Lett.*, 2006, **6**, 2690–2695.
18 G.-R. Li, Z.-P. Feng, Y.-N. Ou, D. Wu, R. Fu and Y.-X. Tong, *Langmuir*, 2010, **26**, 2209–2213.
19 G. H. Yuan, Z. H. Jiang, A. Aramata and Y. Z. Gao, *Carbon*, 2005, **43**, 2913–2917.
20 T. P. Gujar, V. R. Shinde, C. D. Lokhande, W. Y. Kim, K. D. Jung and O. S. Joo, *Electrochem. Commun.*, 2007, **9**, 504–510.
21 R. K. Selvan, I. Perelshtein, N. Perkas and A. Gedanken, *J. Phys. Chem. C*, 2008, **112**, 1825–1830.
22 K. Wang, J. Huang and Z. Wei, *J. Phys. Chem. C*, 2010, **114**(17), 8062–8067.
23 K. S. Ryu, K. M. Kim, N. G. Park, Y. J. Park and S. H. Chang, *J. PowerSources*, 2002, **103**, 305–309.
24 M. Mastragostino, C. Arbizzani and F. Soavi, *J. Power Sources*, 2001, **97–98**, 812–815.
25 M. D. Stoller, S. Park, Y. Zhu, J. An and R. S. Ruoff, *Nano Lett.*, 2008, **8**, 3498–3502.
26 Y. Wang, Z. Shi, Y. Huang, Y. Ma, C. Wang, M. Chen and Y. Chen, *J. Phys. Chem. C*, 2009, **113**, 13103–13107.
27 S. Biswas and L. T. Drzal, *ACS Appl. Mater. Interfaces*, 2010, **2**, 2293–2300.
28 (*a*) Z.-S. Wu, W. Ren, D.-W. Wang, F. Li, B. Liu and H.-M. Cheng, *ACS Nano*, 2010, **4**, 5835–5842; (*b*) J. X. Zhu, T. Zhu, X. Z. Zhou, Y. Y. Zhang, X. W. Lou, X. D. Chen, H. Zhang, H. H. Hng and Q. Y. Yan, *Nanoscale*, 2011, DOI: 10.1039/C0NR00744G.
29 H. Wang, H. S. Casalongue, Y. Liang and H. Dai, *J. Am. Chem. Soc.*, 2010, **132**, 7472–7477.
30 C. Wang, D. Li, C. O. Too and G. G. Wallace, *Chem. Mater.*, 2009, **21**, 2604–2606.
31 A. Abouimrane, O. C. Compton, K. Amine and S. T. Nguyen, *J. Phys. Chem. C*, 2010, **114**, 12800–12804.
32 C. M. Ban, Z. C. Wu, D. T. Gillaspie, L. Chen, Y. F. Yan, J. L. Blackburn and A. C. Dillon, *Adv. Mater.*, 2010, **22**, E145–E149.
33 X. Du, C. Y. Wang, M. M. Chen, Y. Jiao and J. Wang, *J. Phys. Chem. C*, 2009, **113**, 2643–2646.
34 Y.-H. Kim and S.-J. Park, *Curr. Appl. Phys.*, 2010, DOI: 10.1016/j.cap.2010.08.018.
35 H. Wang, L.-F. Cui, Y. Yang, H. Sanchez Casalongue, J. T. Robinson, Y. Liang, Y. Cui and H. Dai, *J. Am. Chem. Soc.*, 2010, **132**, 13978–13980.
36 J. Yan, Z. Fan, T. Wei, W. Qian, M. Zhang and F. Wei, *Carbon*, 2010, **48**, 3825–3833.
37 G. Zhou, D.-W. Wang, F. Li, L. Zhang, N. Li, Z.-S. Wu, L. Wen, G. Q. Lu and H.-M. Cheng, *Chem. Mater.*, 2010, **22**, 5306–5313.
38 S. Q. Chen and Y. Wang, *J. Mater. Chem.*, 2010, **20**, 9735–9739.
39 D. Wang, R. Kou, D. Choi, Z. Yang, Z. Nie, J. Li, L. V. Saraf, D. Hu, J. Zhang, G. L. Graff, J. Liu, M. A. Pope and I. A. Aksay, *ACS Nano*, 2010, **4**, 1587–1595.
40 J. Yan, Z. J. Fan, T. Wei, W. Z. Qian, M. L. Zhang and F. Wei, *Carbon*, 2010, **48**, 3825–3833.
41 W. S. Hummers and R. E. Offeman, *J. Am. Chem. Soc.*, 1958, **80**, 1339–1339.
42 H. A. Becerril, J. Mao, Z. Liu, R. M. Stoltenberg, Z. Bao and Y. Chen, *ACS Nano*, 2008, **2**, 463–470.
43 Z. Wang, X. Zhou, J. Zhang, F. Boey and H. Zhang, *J. Phys. Chem. C*, 2009, **113**, 14071–14075.
44 S. Stankovich, D. A. Dikin, R. D. Piner, K. A. Kohlhaas, A. Kleinhammes, Y. Jia, Y. Wu, S. T. Nguyen and R. S. Ruoff, *Carbon*, 2007, **45**, 1558–1565.
45 Z. Zhang, F. Zhou and E. J. Lavernia, *Metall. Mater. Trans. A*, 2003, **34**, 1349–1355.
46 S. Dubin, S. Gilje, K. Wang, V. C. Tung, K. Cha, A. S. Hall, J. Farrar, R. Varshneya, Y. Yang and R. B. Kaner, *ACS Nano*, 2010, **4**, 3845–3852.
47 L. J. Cote, R. Cruz-Silva and J. Huang, *J. Am. Chem. Soc.*, 2009, **131**, 11027–11032.
48 N. L. Wu, S. Y. Wang, C. Y. Han, D. S. Wu and L. R. Shiue, *J. Power Sources*, 2003, **113**, 173–178.
49 P. Simon and Y. Gogotsi, *Nat. Mater.*, 2008, **7**, 845–854.
50 Q. Y. Yan, R. J. Gambino and S. Sampath, *IEEE Trans. Magn.*, 2004, **40**, 3346–3351.
51 A. Di Fabio, A. Giorgi, M. Mastragostino and F. Soavi, *J. Electrochem. Soc.*, 2001, **148**, A845–A850.
52 X. Zhao, C. Johnston and P. S. Grant, *J. Mater. Chem.*, 2009, **19**, 8755–8760.
53 K. Zhang, L. L. Zhang, X. S. Zhao and J. Wu, *Chem. Mater.*, 2010, **22**, 1392–1401.